

Linking radiomics PET features with metabolic tissue parameters using a mathematical model of tumor growth

Hailey S. H. Ahn¹, Yas O. Yazdi^{1,2}, Brennan Wadsworth²,
Kevin Bennewith², Arman Rahmim^{1,2}, Ivan S. Klyuzhin^{1,2,*}

¹University of British Columbia, Vancouver, BC, Canada

²BC Cancer Research Institute, Vancouver, BC, Canada

*Corresponding author; E-mail: ivan.corr@outlook.com

Cancers often manifest large variations in tumor phenotypes due to genetic and microenvironmental factors. This motivates development of quantitative radiomics-based image analysis, with the aim to robustly classify tumor phenotypes in-vivo and subsequently select most effective treatment regimens. Positron emission tomography (PET) imaging can be particularly helpful in elucidating the metabolic profiles of tumors. However, the relatively low resolution, high noise, and limited data availability of PET make it difficult to link feature values with specific tumor microenvironment properties, and identify which radiomics features are sufficiently robust and sensitive for subtle phenotype discrimination.

In this work, we propose a new method to address these challenges. We use a hybrid, multiscale, stochastic mathematical model of tumor growth to generate simulated cross-sections of tumors in vascularized normal tissue. The model includes a grid for cells of different types and blood vessels, as well as partial differential equation grids for simulation of nutrient diffusion. The generated time-sequences of cell grids are then converted to PET images with realistic resolution and noise. By changing the biological parameters of the model, distinct tumor phenotypes can be obtained, with corresponding PET images.

To demonstrate the utility of our method, we simulate 6 distinct tumor phenotypes including those with hypoxic and necrotic cores, and compute 22 Haralick features of texture that are available in the standardized Pyradiomics library. We identify which features can best discriminate the phenotypes under different noise levels. We demonstrate that together, “Sum entropy” and “Contrast” can reliably detect simulated normoxic, hypoxic, and necrotic phenotypes in PET noisy images, which are difficult to distinguish visually. Our results show that radiomic analysis can be beneficial even in small lesions with diameter of 3.5-4 resolution units, corresponding to 8.7-10.0 mm in state-of-the-art PET scanners.

Introduction

Cancer is classified as a set of diseases related to uncontrolled cell proliferation and has been one of the leading causes of death globally [1]. Various hallmarks of cancer, including resistance to cell death, genetic diversity, vascular network reconstruction, and dynamic tumor tissue microenvironment, result in distinct tumor phenotypes with significant heterogeneity between and within tumors. Increasing evidence shows that highly heterogeneous tumors tend to exhibit more aggressive progressions and are more resistant to treatment, making it difficult to treat with conventional therapy types. Moreover, tumors with similar heterogeneous properties have shown similar progression patterns and sensitivity to treatment despite manifesting tissues at different locations [2–4]. Despite the inherent variability in tumor phenotypes, even for the same type of cancer, the de-facto standard of care follows the "one-size-fits-all" approach wherein a standard dose is delivered to most patients. However, it has been shown that such approach only works satisfactory for 25% of patients [5]. The growing field of precision medicine aims to tackle this problem and make a shift towards personalized treatments for each patient, including a larger role of imaging and radiomics [6].

Given a sufficiently large tumor size, positron emission tomography (PET) imaging with tracer ^{18}F -fluorodeoxyglucose (FDG), a glucose analog, can be used to assess the metabolic heterogeneity of tumors in-vivo. Careful extraction and combination of radiomic features from PET images that describe tumor shape, texture, and morphology, can provide meaningful information relating to tumor heterogeneity. For instance, in a tumor texture analysis study by Orlhac et al., several texture indices were highly correlated with the molecular volume across 3 tumor types [4]. Another study by Hatt et al. [3] showed that heterogeneity quantification in 5 different tumor types had prognostic value for clinical decisions. Indeed, imaging-derived radiomic signature can assist in cancer diagnosis, prognosis, and treatment planning that is not just specific to each patient, but to each distinct tumor [7].

Despite numerous research studies on leveraging PET radiomics in different cancer types, there is a lack of understanding of how the observable (measurable) tumor heterogeneity in PET images, expressed in radiomic feature values, are linked to the properties of tumor microenvironments. Additionally, due to ethical and other reasons, there is a lack of longitudinal data showing how the PET radiomic signatures of tumors change over time with tumor growth without treatment interventions.

To address these limitations, here we develop a new methodology to probe the relationship between microscopic tumor properties and macroscopic radiomic features, and to investigate the expected change in radiomic features with tumor evolution. We employ a hybrid, multiscale mathematical model of tumor growth in vascularized tissue [8] to generate realistic spatial distributions of cells that are, in turn, converted to synthetic PET images showing glucose metabolism. The model is hybrid in the sense that it combines 1) grids of agents, namely autonomous decision-making entities representing different cell types and blood vessels, and 2) partial differential equation (PDE) grids to simulate the nutrient diffusion and exchange. The model uses realistic biological parameters and constants, such as diffusion coefficients, cell size, and cell cycle duration, as well as well-established metabolism models. We are able to generate continuous time-sequences of agent (cell) maps and convert them to PET parametric images of pseudo-standardized uptake values (pSUV), in order to study any PET radiomic feature as a function of model parameters and time.

In this paper, we describe the proposed method in detail, and list the values of model's microparameters that we obtained from previous biological, biochemical, and histological studies. To demonstrate the utility of the method, we generate longitudinal synthetic PET images of 6 distinct tumor phenotypes obtained by varying the model's microparameters such as blood vessel density, their spatial arrangement, and vascular network alteration by tumor cells. We select the optimal set of radiomic features for phenotype differentiation and tumor progression tracking, under realistic resolution and noise conditions. We demonstrate that using specific pairs of radiomics features, all 6 generated phenotypes can be numerically distinguished within 1-cm tumors under realistic resolution and noise. This includes tumors that are nearly indistinguishable to the naked eye.

Methods

Tumor growth simulations

Simulations of tumor growth in vascularized tissue were carried out on a microscopic level using a previously-proposed hybrid multiscale mathematical model [8]. The model combines agents and PDEs to simulate tissue properties and individual cell behavior, which depends on the local state of the tissue microenvironment. The unique advantage of the hybrid model is that any combination of agent grids and PDE grids can be used, allowing layers of complexity in the model (e.g. they can incorporate drugs and/or radionuclides). Furthermore, the components execute independently while the data is easily interfaced between the PDE grids, which enables varying spatial and temporal scales to describe the biological processes involved in solid tumor growth. This is key to modeling tumor growth as tumor tissue is dynamic and complex, with continuous interactions with its microenvironment. The interplay between the agents and the PDE grids defines the tumor characteristics and progression patterns in the simulations, resulting in distinct tumor phenotypes.

The agent types in the model are blood vessels, normal (healthy) cells, and three different states of cancer cells categorized as normoxic, hypoxic, and necrotic (Fig. 1A). Agents occupy identical sized pixels ($20 \times 20 \mu\text{m}$) on a 2D on-lattice agent grid and they are unstackable, meaning that only one agent is allowed in a pixel at a time. Blood vessels act as the sources of nutrients that diffuse from the vessels to tissue. Cancerous and normal cells consume the nutrients (oxygen and glucose) to produce ATP, and the rate of ATP production determines the cell behavior. The PDE grids are used to: 1) update the concentration of nutrients at each grid location from one simulation step to the next, and 2) compute the concentration differentials resulting from diffusion of molecules and consumption by cells.

Diffusion of molecules in tissue follows Fick's diffusion law with distinct diffusion coefficients (D) associated with each type of molecule:

$$\frac{\partial C}{\partial t} = D \nabla^2 C + f \quad (1)$$

where C is the local concentration, and f is the consumption rate specific to each molecule. The consumption rate of a molecule follows the Michaelis-Menten model that describes the enzyme kinetics of oxygen and glucose given by:

$$f = -V_{max} * \frac{[S]}{K_M + [S]}, \quad (2)$$

where f is the rate of consumption, V_{max} is the maximum rate, $[S]$ is the substrate concentration, and K_M is the concentration at half maximum. Deviations in V_{max} and K_M reflect the upregulated metabolism in cancer cells compared to normal cells.

Oxygen consumption rate was simplified to a constant value for each cell type as K_M for oxygen in tissue is negligible compared to the oxygen concentration in tissue ($K_M \ll [S]$):

$$f = -V_{max} * \frac{[S]}{K_M + [S]} = -V_{max} \quad (3)$$

Knowing the consumption rates for oxygen and glucose, we can calculate the ATP production rates. Aerobic respiration yields ~ 27 ATP/glucose, yet tumor cells with altered metabolism utilize glycolysis as the predominant pathway, producing 2 ATP/glucose. Thus, the total ATP production rate is given by,

$$f_{ATP} = -(2f_G + \frac{27f_O}{5}). \quad (4)$$

The ATP production rate for each cell determines the actions available to that cell in every simulation step, as elaborated below.

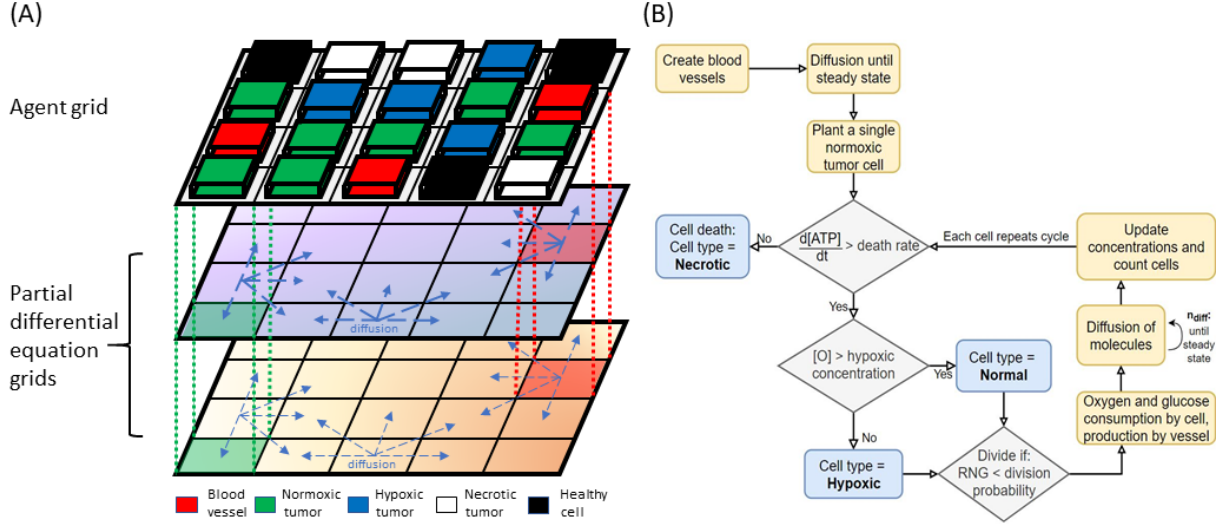


Figure 1: (A) Components of the hybrid mathematical model used in the simulation. The model uses a combination of one agent grid and two PDE grids, as shown. The dashed vertical lines illustrate the link between the agent and PDE grids. Blocks of different color represent different types of agents, and arrows indicate diffusion processes in the PDE grids. Blood vessels act as sources of nutrients. (B) Flowchart of the main algorithm for tumor growth simulation. The steps of simulation initialization, cell type determination, and the processes involved in the change of nutrient concentrations are described. $[O_2]$ is the oxygen concentration at the cell location and n_{diff} is the number of diffusion steps required to reach steady state for each cell step.

Simulation steps

Utilizing one of the advantages of the hybrid model, different temporal scales were used for the agent grid and the PDE grids. Each simulation step in the agent map corresponded to 1 biological hour, where the individual cells determine their cell type and the action to be taken between each iteration. Diffusion of molecules, on the other hand, had a much smaller time scale between each step (30 ms of biological time) which was restricted by the upper limit of the unitless diffusion coefficient in the model where the partial differential equations remain numerically stable. The resulting simulation step thus corresponded to one cell step and multiple diffusion steps; the number of diffusion steps was sufficiently large to reach a steady state in nutrient concentrations between each cell step.

At the beginning of simulation, the agent grid was entirely occupied by normal cells blood and vessels represented as cross-sectional points (Fig. 1B). Several iterations of the diffusion simulation were then applied to allow nutrients to diffuse from blood vessels and reach steady concentrations throughout the PDE grids.

It is believed that tumors originate from a single cell that has accumulated critical genetic mutations through interactions with its microenvironment [9]. This cell progresses into a malignant solid tumor causing destruction of normal tissue, organ failure, and impairment of normal biological functions. Hence, to initiate the tumor growth after a steady state in nutrient concentrations has been reached, we placed a single normoxic cancer cell at the center of the grid.

Next, the behavior of the cell is determined by the local oxygen and glucose concentrations from the corresponding location in the PDE grids. First, conditions are evaluated for cell survival. Cell death can occur in two ways: apoptosis and necrosis. Apoptosis refers to programmed cell death that is necessary for discarding unwanted cells that include aged and defective cells. Necrosis, on the other hand, is induced

by external factors such as nutrient deficiency, radiation, and trauma. Since normal apoptosis is typically disrupted in cancer cells, our model only includes necrosis caused by deficiency in glucose and/or oxygen supply. Biologically, a cell can become necrotic if the ATP production rate is below the threshold level for a prolonged period of time, or when the oxygen concentration falls below 0.5% [O_2]. To reflect this in the model, we introduce a variable cell death probability that depends on the critical value for oxygen concentration and ATP production levels:

$$1 - [(local\ value)/(critical\ value)]^x \quad (5)$$

where x is a variable power. When oxygen or ATP production levels fall below the critical level and the random number sampled between 0–1 is less than the death probability, the cell is deemed necrotic. Once a cell enters the necrotic state, it does not consume any nutrients or go through further division.

After the survival determination, it is tested if the cell should enter a hypoxic state. A cell was determined hypoxic if the oxygen concentration in the corresponding location on the PDE grid was in the range of 1.5–3% [O_2].

In the next step, if adequate nutrient supply was available, viable cells (normoxic and hypoxic) could divide into adjacent locations available in the Moore neighborhood of the agent grid, producing a daughter cell of the same type and kinetic parameters for metabolism. Available locations for producing a daughter cell included pixels occupied by normal cells and vessels; vessel location is chosen only when there is no other available location in its neighborhood. Cell division probability was implemented so that a cell in normoxic conditions would on average divide once every 24 biological hours. Other cells with lower oxygenation had a division probability that scaled proportionally with the local oxygen concentration, with a maximum probability equal to normoxic cells. If the concentrations are over the threshold level and the random number generated falls within the division probability, the cell will go through division. Using the above sequence, the state of all agents on the agent grid was updated in each agent simulation step. After each agent grid update, multiple diffusion simulation steps were taken to reach the new steady-state of nutrient concentration. Thus, from the point of view of the agent grid, the nutrient concentrations are always in a steady state, which is a reasonable assumption given the vastly different timescales of the molecular diffusion and cellular life cycle.

Model parameters and implementation

For computation of nutrient supply, diffusion, and consumption rate by cells, the model used a number of biological parameters such as oxygen and diffusion coefficient in tissue, cell size, and metabolic rate constants. A list of biological constants used in the model are shown in Table 1.

The agent grid pixel size was chosen based on the typical cell size of 20×20 μm and the 2D simulation grids were 1000×1000 pixels corresponding to 2 cm in length and width. The placement of blood vessels on the grid was either random or uniform with small deviations, depending on the simulated phenotype. To minimize edge effects coming from a finite grid size, we imposed periodic boundary conditions on the nutrient concentration PDE grids to simulate a section of a larger tissue.

Tested model alterations

Since blood supplies oxygen and glucose, blood vessel density and their spatial distribution in tissue play an essential role in shaping the local microenvironment, and consequently the phenotype of a growing tumor.

Thus, to simulate different tumor phenotypes, we adjusted the following tissue microparameters of the model: a) blood vessel density, b) vessel removal (obstruction) probability, c) vessel distribution pattern, and d) cell death probability from depletion of nutrients. In total, six different phenotypes were simulated, with the respective parameter values given in Table 2. The first three phenotypes only included oxygen

Biological constant	Values
Average cell (unit) size	$20 \mu m$
Average time for aerobic cell division	24 hours
Capillary density range	20-100 mm^2 [10-12]
Oxygen diffusion coefficient in tissue	$1.65 \times 10^{-5} cm^2/s$ [13]
Glucose diffusion coefficient in tissue	$2.7 \times 10^{-6} cm^2/s$ [14]
Oxygen flux from capillary	$2.81 \times 10^{-12} mol/min/unit$ [15]
Glucose concentration in capillary	$5 \times 10^{-3} mol/L$
Oxygen consumption rate - normal tumor	$4 \times 10^{-15} mol/min/cell$ [16]
Oxygen consumption rate - hypoxic tumor	$2 \times 10^{-15} mol/min/cell$ [17]
Oxygen consumption rate - non-cancer cell	$2.5 \times 10^{-18} mol/min/cell$ [15]
Glucose V_{max} - normal tumor	$5 \times 10^{-14} mol/min/cell$
Glucose V_{max} - hypoxic tumor	$1.02 \times 10^{-13} mol/min/cell$
Glucose V_{max} - non-cancer cell	$5 \times 10^{-15} mol/min/cell$
Glucose K_M	$2 \times 10^{-14} mol/min/cell$
Death ATP production rate	$2.57 \times 10^{-14} mol/min/cell$

Table 1: Model biological constants

PDE grid (to focus on the effects of hypoxia), while the last three phenotypes included both oxygen and glucose PDE grids.

Vessel removal probability is the probability that a dividing cancer cell replaces a vessel in its neighborhood, only if all of the surrounding grid locations are occupied by cancer cells. This parameter characterizes the degree of vascular network alteration by tumor cells.

Necrotic death probability reflects the probability of necrosis due to prolonged ATP depletion in the local tissue, and R is the ratio of local ATP production rate to critical ATP production rate below which necrosis becomes possible. Varying this parameter indicates the specific cell population's resistance to external stress, in this case lack of nutrients.

Other parameters such as vascular nutrient concentration, diffusion coefficients in tissue, and maximum metabolic rates for each cell type were set to a fixed value in all simulations within a realistic physiological range (Table 1).

Five realizations of longitudinal growth were simulated for each phenotype. All simulations started with a single cancer cell placed at the center of the agent grid, and continued until the total number of cells surpassed the minimum number of cells required to fill a circle of radius 1 cm. During the simulations, the state of the agent grid at every 10 hours of biological time was exported as TIFF images, where pixel RGB values represented different cell types. The resulting 30 (6 phenotypes \times 5 realizations) time series of images were used to generate synthetic PET images for radiomics analysis.

Conversion of agent maps to synthetic PET images

To convert agent maps to synthetic pSUV images, we make an approximation that for each cell, the tracer (presumed to be FDG) uptake depends only on the type and metabolic rate of the cell; thus, we neglect possible effects of restricted blood supply and endogenous-exogenous competition.

Assuming that normal healthy tissues have a pSUV of ~ 1.0 , the pSUVs for different states of cancer cells can be obtained from their relative glucose consumption rates. Oxygenated tumor cells show about 8 times higher uptake than normal cells [18], and hypoxic tumor cells display about 1.5 times enhanced uptake compared to oxygenated tumor cells [19, 20]. Necrotic cells do not consume glucose. Thus, the pSUV values were set to 0, 1, 8, and 12 for necrotic, normal, oxygenated tumor, and hypoxic tumor cells, respectively. Using these assignments, time-sequences of cell-level parametric pSUV images (1000×1000

Phenotype	Vessel density [mm-2]	Vessel removal Probability	Vessel distribution pattern	Necrotic death probability
Type O1	20	1	Random	$1 - R$
Type O2	100	1	Uniform density	$1 - R$
Type O3	20	0.05	Random	$1 - R$
Type OG1	20	1	Uniform density	$1 - R^2$
Type OG2	100	0.05	Uniform density	$1 - R$
Type OG3	20	0.05	Uniform density	$1 - R^2$

Table 2: Model variable parameters specific to each tumor phenotype. The variable R is the ratio of local ATP production rate to death production rate.

pixels, pixel size 0.02 mm) were generated from the sequences of agent maps.

To simulate realistic PET resolution and noise, each pSUV image was scaled to the units of activity concentration, forward-projected into a sinogram space with added Poisson noise, and reconstructed using ordered-subset expectation maximization (OSEM) with pixel size 0.58 mm and resolution 2.35 mm full-width at half-maximum (FWHM). The reconstructed image dimensions were 34×34 pixels. The forward-projection and reconstruction was performed using a publicly-available (https://github.com/ashrafinia/PET_sim_recon) and previously published [21] image reconstruction framework written in Matlab.

Post-reconstruction image noise was measured using a uniform reference image with pSUV set to 2.37, which modeled the average FDG uptake in the liver [22]. We adjusted the simulation and reconstruction parameters to obtain images with 5%, 10%, and 15% noise, measured in units of normalized standard deviation (NSTD). These noise levels cover the range of noise typically observed in clinical scans and measured over the liver [23].

Radiomic features

For each simulated PET image in the time sequences, we computed all 22 Haralick features (HF) that are available in the Pyradiomics framework [24], which is compliant with the Image Biomarker Standardization Initiative (IBSI) [25]. These features included Autocorrelation, Joint Average, Cluster Prominence, Cluster Shade, Cluster Tendency, Contrast, Correlation, Difference Average, Difference Entropy, Difference Variance, Joint Energy, Joint Entropy, Imc1, Imc2, Inverse difference moment, Inverse difference moment normalized, Inverse difference, Inverse difference normalized, Inverse variance, Maximum probability, Sum Entropy, and Sum of Squares. The features were computed from the gray level co-occurrence matrix (GLCM, 2.5D, merged). The pixel intensities were quantized using the constant bin size technique, as per IBSI and Pyradiomics recommendations. The pixel dimensions were specified to be isotropic for GLCM computation. All features were extracted within lesion masks without image re-sampling. The masks were pre-processed to contain a single connected region without holes. The features were computed at every 10 hour biological time step to see the progression of each feature value with tumor growth.

Analysis

First, to validate the model, we analyze the resulting tumor phenotypes using the sequences of agent maps, and measure tumor growth parameters such as the growth rate and concentration of nutrients in the tissue during tumor growth. We characterize the fractions of normoxic, hypoxic, and necrotic cells in each phenotype, and compare the observed patterns with real histopathology images.

Second, we analyze radiomic features computed from synthetic PET images as functions of tumor growth. Using the t-scores, we measure the ability of different features to discriminate between pheno-

types, for a) varying lesion sizes, and b) varying noise levels.

Finally, we test over 200 of paired feature combinations, to find the optimal pair of features for phenotype discrimination.

Results

Phenotype analysis

The developed tumor growth model was able to simulate tumor progressions of distinct phenotypes resulting from differences in the tumor microenvironment. The agent maps for simulated tumor phenotypes and their microscopic structures are shown in Figure 2. The simulated phenotypes were visually distinct, and manifested a number of features observed in real tumors. Phenotype O1 is highly diffuse and hypoxic, and incorporates the highest amount of healthy tissue. This tumor grows by propagating tendril-like structures, which encapsulate pockets of healthy cells. Phenotype O2 is solid and densely packed, with minimal amounts of necrosis, and with normoxic and hypoxic regions intertwined. Phenotype O3 is most aggressive (i.e. fastest-growing) and diffuse, containing a large fraction of viable normoxic cells.

Phenotype OG1 is characterized by a pronounced necrotic core encompassed by a thin layer of hypoxic tumor cells. Most of the blood vessels inside the OG1 tumors have been replaced by the tumor cells leading to wide-spread necrosis. This is consistent with Thominson's results where necrosis was triggered in cells that were further than 160um from a vessel [26]. In comparison, the less aggressive vessel alteration property in phenotype OG2 spared some working vessels, and thus viable hypoxic cells are more prominent. OG2 does not present a necrotic core but has a more irregular boundary and pronounced hypoxia. Relatively small regions of necrosis are distributed throughout the tumor. In phenotype OG3, some necrosis and hypoxic tumor cells are visible, but the tumor is mostly normoxic with significantly more working vessels. Figure 2 demonstrates that our model is capable of producing a wide range of macroscopic tumor phenotypes in response to changes in the initial conditions and/or model parameters.

Comparison to histology images

To qualitatively evaluate the realism of simulated phenotypes, we compare the simulated cellular patterns to real histology slides obtained from subcutaneous tumor xenografts of well-known cell lines (Fig.3).

Normoxic clusters observed in OG3 around blood vessels can be seen in human cervical squamous cell carcinoma, SiHa line (Fig.3A). Here green color represents region with active perfusion, meaning normoxic regions with adequate nutrient supply (imaged with Hoechst 33342). Blue color represent regions with hypoxia (imaged with pimonidazole without any hypoxia-modifying treatments). Note the similarities in the spatial distribution of normoxic clusters, as well as their size. Necrotic regions are also present in the slide (dark blue color), albeit in lesser quantity compared to the simulation.

In phenotype OG2, a normoxic layer surrounds the tumor; a similar feature can be observed in human colorectal adenocarcinoma, WiDr line (Fig.3B). Green color represents perfusion (imaged with Hoechst 33342), while blue color indicates hypoxia (imaged with pimonidazole). Note the similar thickness of the normoxic layers in the simulated and real images. Small amounts of necrosis are present on the inner sides of simulated and real tumors. Interestingly, hypoxic regions in simulations and real images manifest in similar wave-like patterns. Pockets of healthy tissue found in OG2 are also encountered in real histological images solid tumors, though they are not visible in the shown slide.

Finally, the dense phenotype O2 and necrosis-dominant phenotype OG1 are compared to patterns observed in human cervical squamous cell carcinoma (ME180 line) in Figs.3C and D, respectively. In both cases, green color corresponds to viable cells (imaged with DAPI), blue indicates hypoxia (imaged with pimonidazole), and the red channel was obtained by CD31-staining to highlight blood vessels. In Fig.3C, a dense intertwined pattern of normoxic and hypoxic cells without necrosis can be observed in

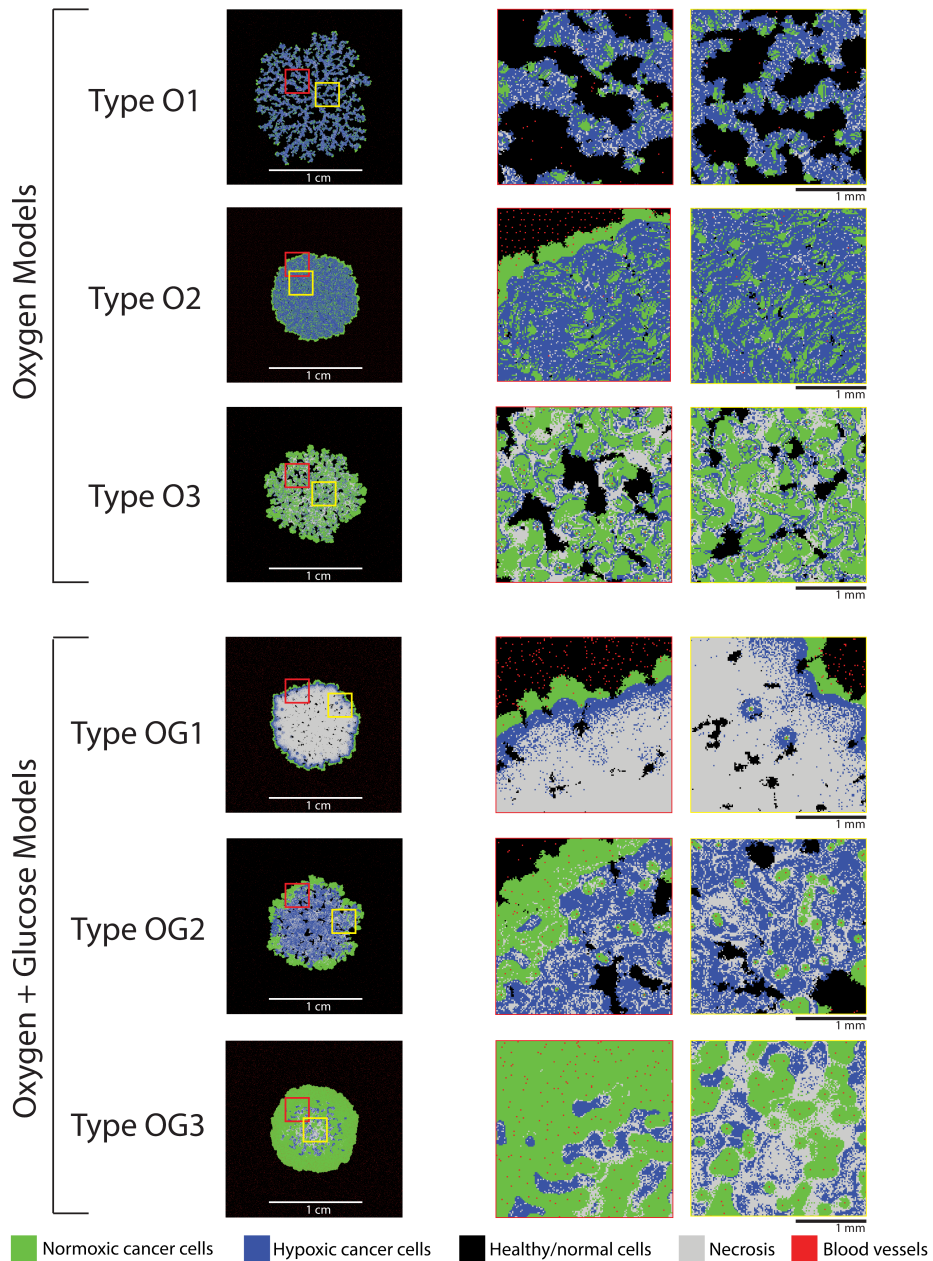


Figure 2: Agent maps showing the distribution of different cell types in the simulated phenotypes, and zoomed-in cutouts. Oxygen models at the top, and oxygen + glucose models at the bottom. Starting from a single cancer cell, growth was simulated until tumors reached ~ 1 cm in diameter.

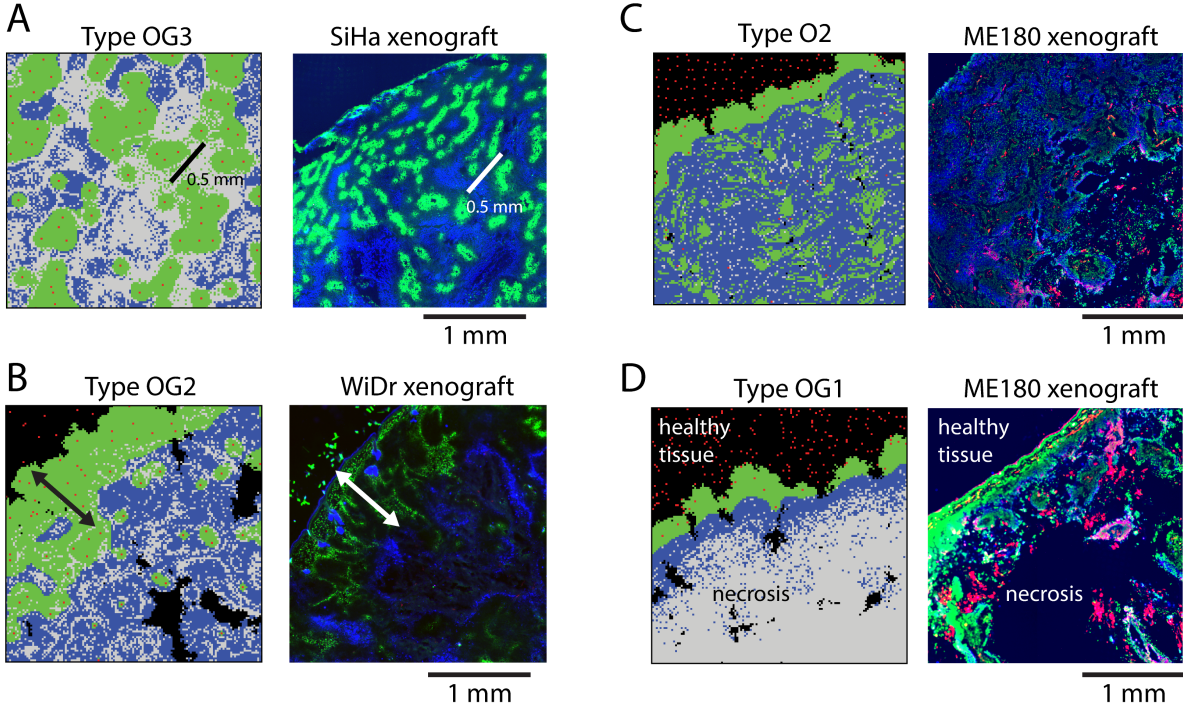


Figure 3: Simulated tumor phenotypes compared to real microscopic images of subcutaneous tumor xenografts. (A) Phenotype OG3 compared to SiHa human cervical squamous cell carcinoma. Line segments compare structures of similar size. (B) Phenotype OG2 compared to WiDr human colorectal adenocarcinoma. Arrows highlight normoxic regions. (C) Phenotype O2 compared to ME180 human cervical squamous cell carcinoma. (D) Phenotype OG1 compared to ME180 human cervical squamous cell carcinoma. Regions of necrosis and areas outside the tumor (healthy tissues) are labeled.

the real image, similar to the pattern found in phenotype O2. In Fig. 3D, a thin layer of normoxic and hypoxic cells separates the outside of the tumor from the necrotic core.

To summarize, cellular patterns that we observed in simulated phenotypes are also encountered in real histology slides of tumors, which strengthens the realism of the model. In the next session, we provide additional quantitative validation of the model.

Quantitative model validation

For quantitative validation of the model, we compare the macroscopic un-controlled model observables, such as tumor growth rates and steady-state nutrient concentrations, to published experimental data. The nutrient concentrations in steady state were achieved entirely through diffusion processes in the PDE grids, and were not predetermined prior to the simulation. Thus, they represent derivative measures of the simulations that can be used for model validation.

The simulated tumors reached the size of ~ 1 cm in diameter within 65–164 days (Fig. ??A), demonstrating realistic growth rates. The average oxygen and glucose concentrations within normal and cancer tissue were measured at the end of each simulation. The average oxygen concentration in normal tissue was 131 mmHg in all six phenotypes, whereas in the tumor tissue, the values varied between 0.585–32.960 mmHg. Glucose concentrations in phenotypes OG1, OG2, and OG3 were also computed and

the values ranged between 2.72–2.96 mM for abnormal tissue and 0.0085–0.777 mM for tumor tissue. The lower end of the value corresponded to type OG1 which exhibits a prominent necrotic core where viable vessels are no longer present. Omitting type OG1, the glucose concentration ranges between 0.187–0.777 mM, which falls within the normal range of glucose concentrations [27, 28].

Simulated PET images

Simulated PET images for fully-grown tumors are plotted in Figure 4. For each phenotype, the same tumor was reconstructed with different noise levels: 5% and 15% represent the minimum and maximum noise typically found in routine imaging, while 10% represents the average noise magnitude [23]. The figure demonstrates that the simulated PET images, particularly at low 5% noise, preserve spatial features that allow for phenotype differentiation. Diffuse phenotypes like O1, O3 and OG2 manifest unique spatial heterogeneity patterns even at resolution that is 100 lower than the underlying agent grid (i.e. 2.35 mm FWHM vs 0.02 mm cell size). The phenotypes can also be visually identified by the tumor intensity, although in reality this will be confounded by a greater-than-simulated variability in the uptake levels (SUVs).

As expected, the phenotype differentiation in PET images becomes more difficult with higher noise. For example, the necrotic core in OG3 is clearly visible at 5% noise and obscured at 15% noise. Likewise, phenotype OG1 becomes virtually indistinguishable from the background at 15% noise.

To illustrate this point further, Figure 5 shows tumors that are size-matched in PET images reconstructed without noise and 10% noise. Simulated images of phenotypes O1 and O3 at 10% noise are visually indistinguishable, as well as phenotypes OG2 and OG3. Better identification of such phenotypes in practice may guide therapy decisions. For example, O1/O3 phenotype differentiation can be linked to the task of hypoxia detection, and G2/G3 differentiation can be linked to necrotic core detection.

In the next section, as an example application of our method, we use our model to find features that can robustly differentiate all 6 simulated phenotypes with noise up to 10%. In addition, we measure the minimum tumor size for those features to be informative.

Radiomic analysis

We analyzed all 22 Haralick texture features available in the PyRadiomics library to find which features can distinguish phenotypes in simulated PET images. For each feature, we ran a t-test between two distributions of feature values, corresponding to two phenotypes. The resulting t-scores for features computed at 10% image noise are given in Table 3. The data demonstrate that different features were optimal for differentiation of different pairs of phenotypes. For example, ClusterProminence worked reasonably well for discriminating all pairs except O1/O3. On the contrary, Imc1 was only effective in differentiating O1/O3, but not other phenotypes. The most difficult phenotypes to differentiate were OG2/OG3, followed by O1/O3; this is consistent with their similar visual appearance (Fig. 5). Thus, in the rest of the analysis, we specifically focus on these 4 phenotypes.

The magnitude of image noise was found to have a strong impact on the value of texture features, and also on their phenotype discrimination performance. For example, per Table 3, in noisy images (10%) the best features to discriminate between phenotypes OG2 and OG3 were ClusterProminence ($t=4.4$), ClusterTendency ($t=4.4$), SumSquares ($t=4.4$), and SumEntropy ($t=3.7$). The best features for O1/O3 discrimination were Contrast ($t=6.6$), JointAverage ($t=6.3$), and Autocorrelation ($t=6.0$). On the other hand, in noise-free PET images, SumEntropy ($t=5.5$) and Correlation ($t=5.1$) were best features for OG2/OG3 discrimination, and DifferenceVariance ($t=11.0$) and DifferenceEntropy ($t=10.3$) were best for O1/O3 discrimination.

The data in Table 3 demonstrate that no single feature was able to differentiate all 6 phenotypes. Thus, classification models to differentiate all phenotypes should include at least 2 variables. To that end, we performed testing of 231 unique feature pairs to select the best pair for noise-resilient phenotype

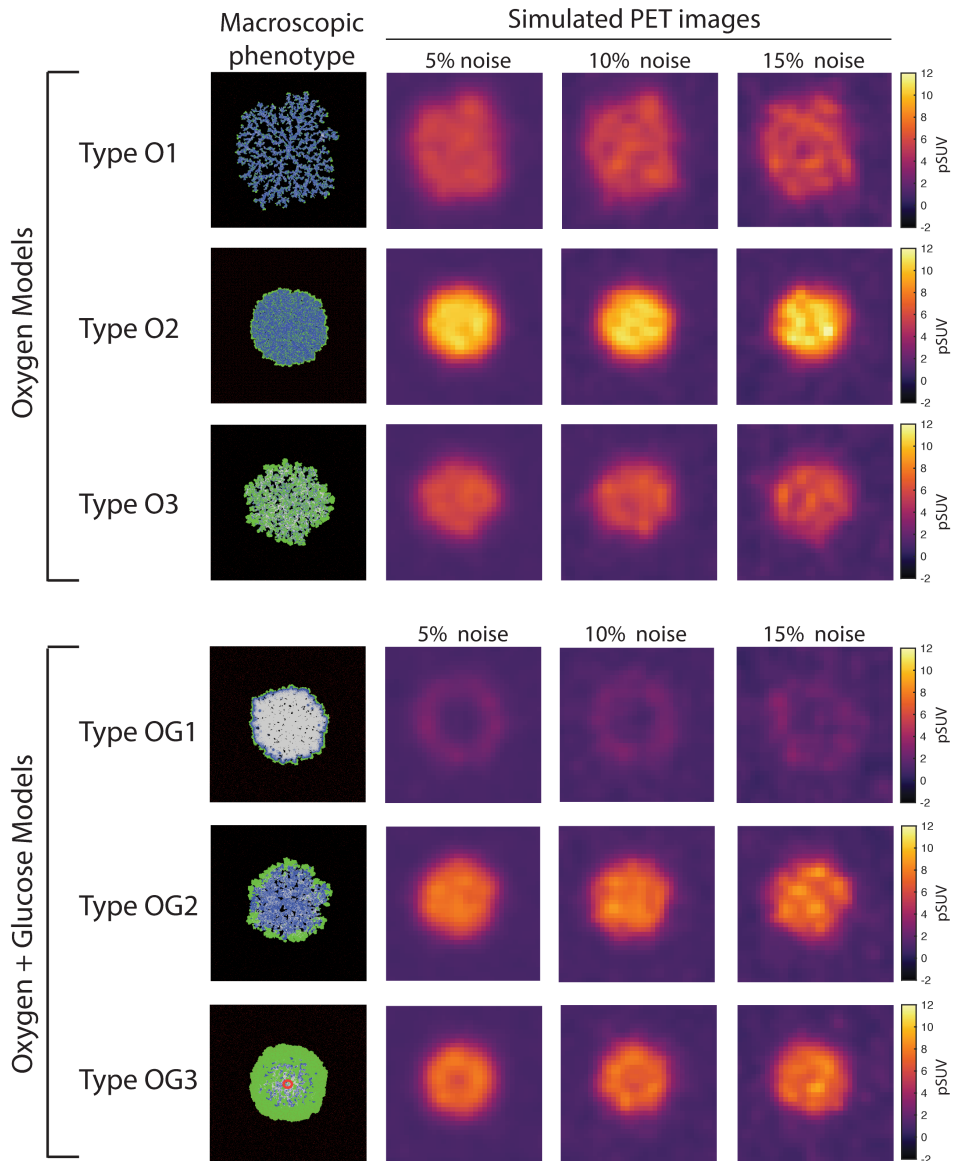


Figure 4: Synthetic PET images produced for the simulated tumor phenotypes, at 5%, 10%, and 15% image noise levels. The agent grids were converted to images of expected FDG uptake, forward-projected into sinogram space with added Poisson noise, and reconstructed with resolution 2.4 mm FWHM. Noise was regulated by adjusting the simulated acquisition time.

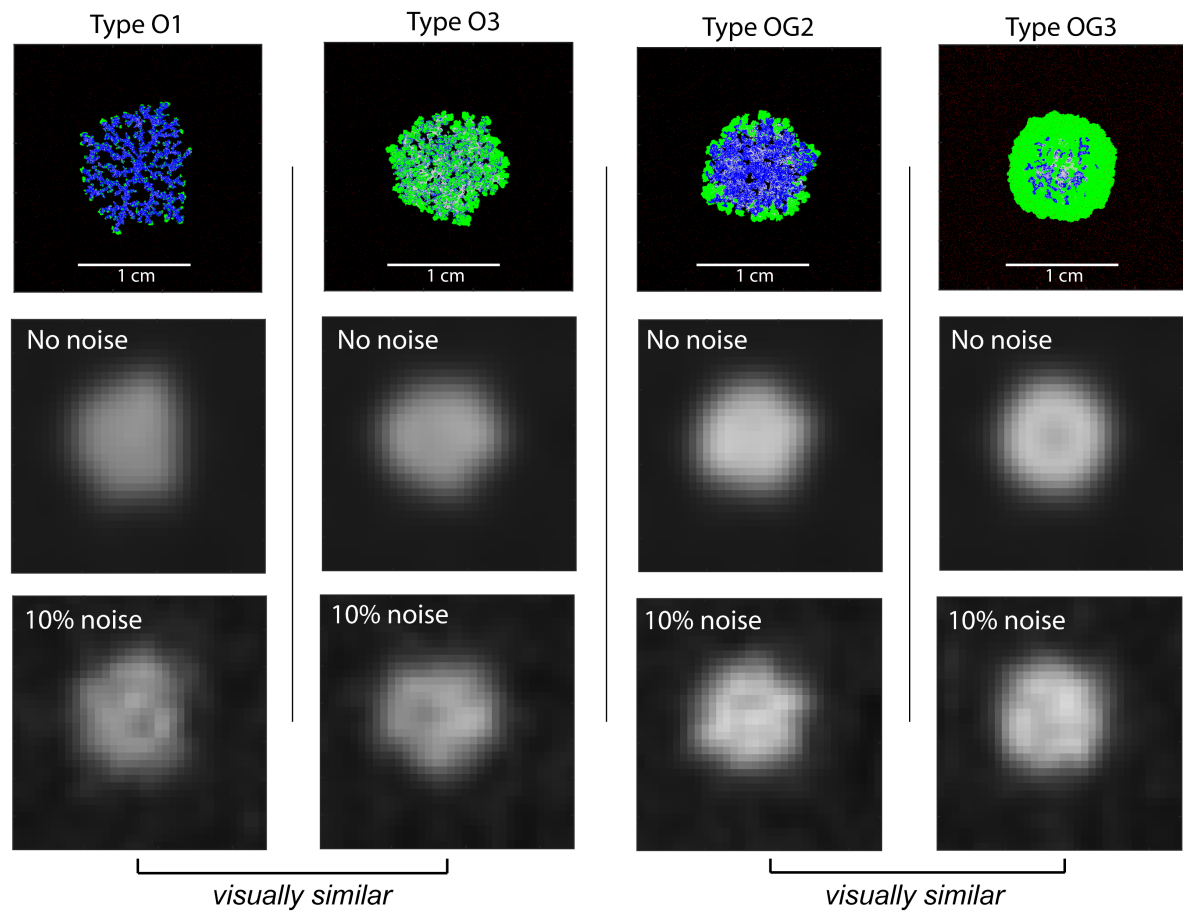


Figure 5: Noise-free and noisy simulated PET images for phenotypes O1, O3, OG2 and OG3. With 10% image noise, O1 is visually similar to O3, and OG2 is visually similar to OG3.

discrimination; this approach also accounts for possible intrinsic correlations between features. We found that a combination of SumEntropy and Contrast was able to classify all 6 simulated phenotypes with high accuracy, with relative image noise levels up to 10% (Fig. 6A). The accuracy of OG2/OG3 phenotype classification was 100% without noise and 80% with 10% noise. The accuracy of O1/O3 phenotype classification was 94% without noise and 94% with 10% noise. All other pairs of phenotypes (e.g. O1/OG2, O3/OG3, etc.) were classified with 100% accuracy. Figure 6A demonstrates that with 15% image noise and above, robust classification becomes problematic.

Longitudinal simulations of tumor growth can help estimate the minimum tumor size requirements for phenotype classification. To demonstrate this, as the last step we analyze how the values of radiomic features change with tumor growth. The graphs of Haralick ClusterProminence, ClusterTendency, Contrast, and SumEntropy against tumor diameter are plotted in Figure 6B. The error bars encapsulate both image noise and differences in tumor appearance in repeated growth trials ($N=5$). We notice that for almost the entire range of studied diameters, there is significant overlap of feature values for phenotype pairs O1/O3 and OG2/OG3. However, above ~ 9 mm tumor diameter, Haralick Contrast can provide statistically significant differentiation between O1 and O3, and SumEntropy can help to differentiate between OG2 and OG3. In our simulations, 9 mm is equivalent to 3.8 resolution units.

Importantly, we find that many features changed non-linearly and non-monotonically with tumor growth. Consider, for example, the values of ClusterProminence for OG3: the feature values will be similar for tumor diameters 5.5 mm and 10 mm, due to the "U"-like shape of the graph. This may have implications for using this feature for measuring the tumor response to therapy. On the other hand, the values of ClusterProminence for O1 and O3 are relatively constant with tumor diameter, which makes this feature a poor choice for tracking the response for those phenotypes. The best features for tumor response and/or progression tracking are those that increase monotonically and have small error bars.

To summarize, our analysis shows that Haralick SumEntropy and Contrast are powerful radiomic features for phenotype differentiation, such as detecting tumors with hypoxia or necrotic cores, when tumor diameters above ~ 9 mm or 3.8 resolution units.

Discussion

We developed a new method to simulate biologically-plausible tumor phenotypes, and their longitudinal development. The proposed method can be used to investigate the interplay between the values of radiomic features and tumor environment and phenotype. Furthermore, the influence of image noise, resolution, and other factors on the descriptive strength of features can be investigated. We demonstrate that our microscopic tumor growth model produces realistic tissue patterns, tumor growth rates, and nutrient concentrations. We likewise demonstrate that very different microscopic phenotypes can produce visually-similar PET images, however it should be possible to create a highly-sensitive classifier with appropriately chosen features.

In comparison to our approach, static radiomics phantoms previously used in literature have several downsides: 1) they do not allow longitudinal studies and lack the temporal dimension, 2) they have simplified geometries that are not reflective of real tumor complexity, 3) they don't provide the means to generate subtle variations of morphology, while keeping overall patterns the same between different phantom realizations, and 4) they are not linked to fundamental underlying biology and microenvironmental factors. In contrast, we believe that the proposed simulation framework will enable new investigations of the interplay between the tumor environment, phenotype, image noise, resolution, and region of interest definitions. It may also guide the development of new features that are informative, robust and reliable, ultimately allowing for more optimized treatment planning and prognosis.

As an example application of the method, we performed optimal feature search for differentiation of hypoxic and necrotic phenotypes in presence of noise. The tested phenotypes were achieved by modifying the blood vessel density, vessel removal probability, vessel distribution pattern, and cell death probability

	OG 1 vs OG2	OG2 vs OG3	OG1 vs OG3	O1 vs O2	O2 vs O3	O1 vs O3
Autocorrelation	25.2	0.9	20.0	22.6	21.4	6.0
JointAverage	27.0	0.6	22.6	25.6	24.2	6.3
ClusterProminence	19.4	4.4	16.4	19.3	18.8	2.2
ClusterShade	18.7	1.2	20.6	12.4	12.0	2.3
ClusterTendency	23.6	4.4	20.8	21.5	21.6	1.2
Contrast	18.0	1.3	24.8	56.2	49.5	6.6
Correlation	7.0	2.2	4.8	0.5	3.8	2.0
DifferenceAverage	22.5	2.1	24.1	25.0	20.5	5.3
DifferenceEntropy	20.6	0.5	24.4	39.3	36.5	4.3
DifferenceVariance	14.1	0.2	19.3	15.7	14.0	2.8
JointEnergy	6.4	2.7	5.8	5.0	4.4	0.9
JointEntropy	16.5	3.0	16.1	10.3	8.9	1.8
lmc1	0.8	1.6	3.0	1.1	3.3	3.8
lmc2	7.9	3.4	6.5	9.0	10.1	0.2
ldm	20.9	2.4	19.3	12.3	9.1	3.8
ldmn	1.7	0.7	1.6	1.2	1.8	1.0
ld	18.9	2.2	17.3	11.4	8.2	3.3
ldn	2.3	0.7	1.9	3.5	3.2	0.0
InverseVariance	3.5	0.1	3.0	7.3	6.7	0.1
MaximumProbability	4.8	2.2	4.2	2.2	2.0	0.1
SumEntropy	14.7	3.7	13.8	10.3	9.0	1.0
SumSquares	24.6	4.4	22.4	22.5	22.5	1.4

Table 3: t-scores for discrimination between pairs of phenotypes, rows correspond to different Haralick features. Values with $p \leq 0.01$ are highlighted in bold.

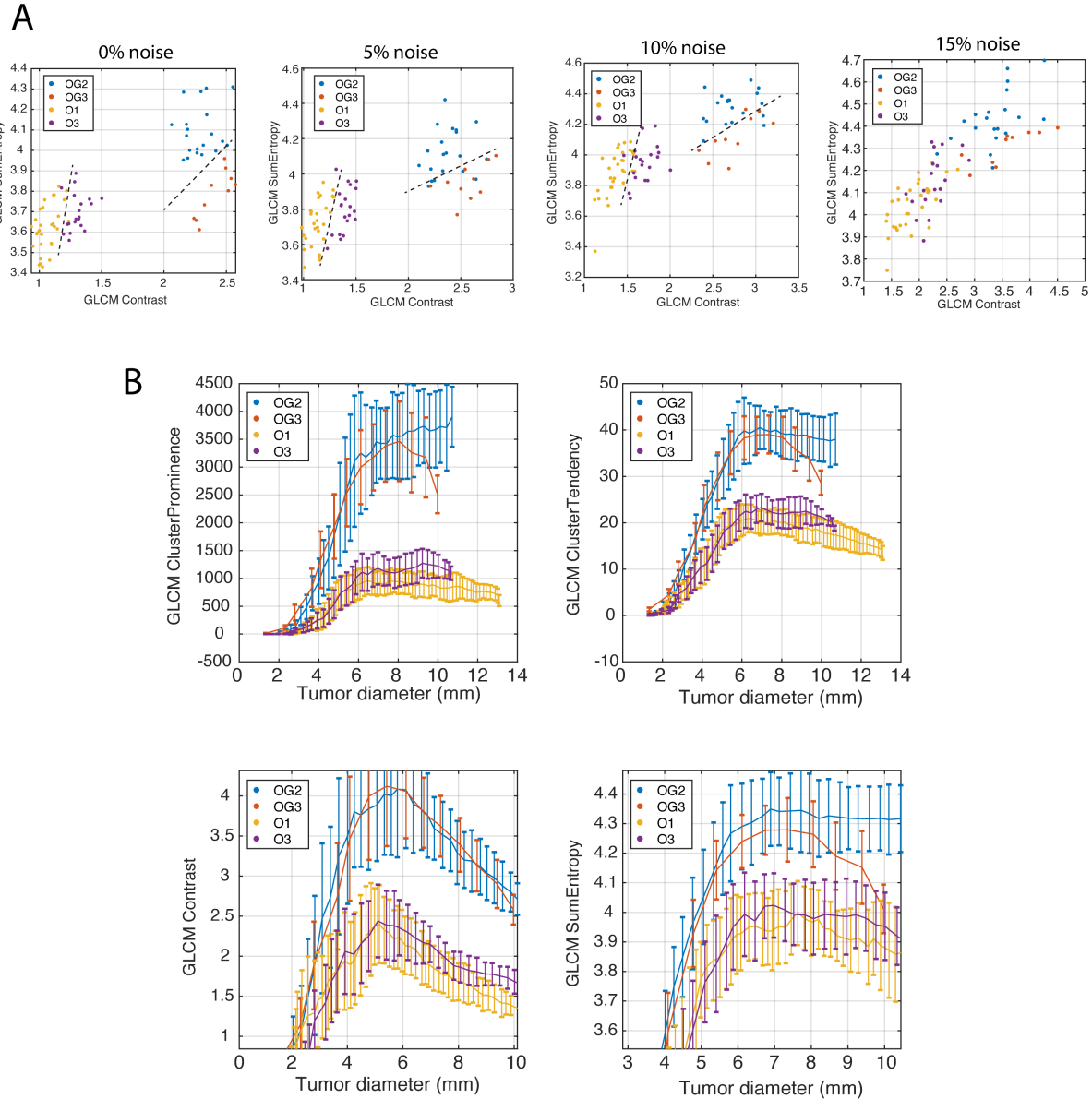


Figure 6: (A) Together, GLCM SumEntropy and GLCM Contrast are able to identify all 6 phenotypes with image noise up to 10% (data for phenotypes OG1 and O2 are outside of the plot bounds). (B) A representative set of Haralick features plotted as functions of tumor size (longitudinal tumor growth).

from depletion of nutrients (resilience to stress). We demonstrated that not a single feature among 22 tested can differentiate all 6 phenotypes, thus at least 2 features are needed for accurate phenotype classification. This finding highlights the importance of multi-variate analysis. Standardized Haralick features SumEntropy and Contrast from the widely-used PyRadiomics framework were found to be the most sensitive and noise-resilient features for this task. Our results suggest that radiomic analysis can be beneficial even in small lesions with diameter of 3.5-4 resolution units, to differentiate visually-similar phenotypes. Another important finding is that feature values may change non-monotonically with tumor growth, which may render certain features non-suitable for tracking disease progression or therapy response.

Several model extensions are possible that can enable new directions of studies. The model parameters and initial conditions can be adjusted to simulate countless scenarios; for instance, using different cancer cell types and incorporating other biomolecules that influence tumor growth. Due to the hybrid nature of the tumor growth model, different types of agents and PDE grids can be easily incorporated. Of particular interest may be to incorporate a PDE grid for chemotherapy drugs or radiopharmaceutical molecules, to investigate the absorbed dose and effectiveness of radiopharmaceutical therapy in different tumor types. For the addition of each new molecule, a new PDE grid should be added to the model and the diffusion coefficient in tissue should be specified. The parameters of the agents used in the model can also be adjusted within the biologically reasonable range to simulate different cell lines and genetic variations. Examples of parameters include the vessel removal probability, division rate, and cell death probability, which biologically reflect invasiveness, proliferation rate, and cell resistivity to external stress, respectively. Cancer hallmarks such as angiogenesis and clearing of necrotic regions can be modeled as well. This can be achieved by entering additional functions in a cell decision step to determine whether a cell will create new vessels or replace necrotic cells with normal non-cancerous cells.

Another extension can be the addition of intra-tumor genetic variability and environment pH. Both factors are known to play an important role in tumor resistance to chemotherapy and radiotherapy. In fact, in a previous study conducted by Robertson-Tessi, et al., the authors demonstrated the use of a hybrid mathematical oncology modeling approach by simulating tumor growth in vascularized tissue to assess the effects of tumor microenvironments on tumor phenotypic adaptations [8]. The cells in the model had a continuously variable metabolic phenotype and different resistance to acidic environments, which are both traits that were inherited from the parent to the daughter cells with small variations. Similarly to our approach, point source vasculature was used to represent the vessels crossing the 2D plane delivering nutrients to the tissue. The vessel distribution was altered through angiogenesis or vessel degradation. The effects of the non-uniform microenvironment on acidosis and the development of aggressive traits in acid-resistant cells have been examined. The extent of how tumor heterogeneity affects the effectiveness of chemotherapy has also been assessed through the model. The basic mechanism of our tumor growth model is similar to that of Robertson-Tessi's; however, the central focus here is to link the observable tumor heterogeneity in synthetic PET images to the tumor tissue microenvironment, evaluated using a quantitative radiomics approach. Thus, it should be relatively straightforward to incorporate environmental acidity and genetic variability within our method.

A major limitation of our approach is that it does not include modeling of mechanical forces, such as cell cohesion, tissue resistance to tumor expansion, or blood vessel elasticity. Hence, our approach does not model the effects of shear stress and external pressure. The validity of our simulations are restricted to small tumors embedded in uniform tissue, where the external forces on the growing tumors are expected to be small. Another limitation is that our method has only been tested in 2D. The hybrid automata library offers an option to extend the simulations to a 3D grid, which may be a more realistic model of volumetric cancer (albeit much more computationally expensive). The purpose of the simulation in this study is to assess tumor heterogeneity arising from metabolic heterogeneity and variations in tumor microenvironments, so a 2D slice representing a cross section of the solid tumor was deemed to be sufficient.

Future work will focus on generating additional phenotypes, and further improvement and validation of the model's realism. A "standard database" of phenotypes can be created to be used in PET radiomics studies as advanced phantoms. Another future research direction is the addition of radiopharmaceutical compounds to the simulation, in order to study the effects of phenotype on the absorbed dose.

Acknowledgment

This work was supported by CIHR project grant PJT-162216, and NIH / CIHR Quantitative Imaging Network grant 137993.

References

- [1] Freddie Bray, Jacques Ferlay, Isabelle Soerjomataram, Rebecca L. Siegel, Lindsey A. Torre, and Ahmedin Jemal. Global cancer statistics 2018: Globocan estimates of incidence and mortality worldwide for 36 cancers in 185 countries. *CA: A Cancer Journal for Clinicians*, 68(6):394–424, 2018.
- [2] Paulina E. Galavis, Christian Hollensen, Ngoneh Jallow, Bhudatt Paliwal, and Robert Jeraj. Variability of textural features in fdg pet images due to different acquisition modes and reconstruction parameters. *Acta Oncologica*, 49(7):1012–1016, 2010.
- [3] M. Hatt, M. Majdoub, M. Vallieres, F. Tixier, C. C. Le Rest, D. Groheux, E. Hindie, A. Martineau, O. Pradier, R. Hustinx, and et al. 18f-fdg pet uptake characterization through texture analysis: Investigating the complementary nature of heterogeneity and functional tumor volume in a multi-cancer site patient cohort. *Journal of Nuclear Medicine*, 56(1):38–44, 2014.
- [4] F. Orlhac, M. Soussan, J.-A. Maisonneuve, C. A. Garcia, B. Vanderlinden, and I. Buvat. Tumor texture analysis in 18f-fdg pet: Relationships between texture parameters, histogram indices, standardized uptake values, metabolic volumes, and total lesion glycolysis. *Journal of Nuclear Medicine*, 55(3):414–422, 2014.
- [5] Brian B Spear, Margo Heath-Chiozzi, and Jeffrey Huff. Clinical application of pharmacogenetics. *Trends in molecular medicine*, 7(5):201–204, 2001.
- [6] Philippe Lambin, Ralph TH Leijenaar, Timo M Deist, Jurgen Peerlings, Evelyn EC De Jong, Janita Van Timmeren, Sebastian Sanduleanu, Ruben THM Larue, Aniek JG Even, Arthur Jochems, et al. Radiomics: the bridge between medical imaging and personalized medicine. *Nature reviews Clinical oncology*, 14(12):749–762, 2017.
- [7] Chintan Parmar, Ralph TH Leijenaar, Patrick Grossmann, Emmanuel Rios Velazquez, Johan Bussink, Derek Rietveld, Michelle M Rietbergen, Benjamin Haibe-Kains, Philippe Lambin, and Hugo JW Aerts. Radiomic feature clusters and prognostic signatures specific for lung and head & neck cancer. *Scientific reports*, 5(1):1–10, 2015.
- [8] Mark Robertson-Tessi, Robert J. Gillies, Robert A. Gatenby, and Alexander R.A. Anderson. The importance of metabolic heterogeneity and its consequences on tumor invasion, metastatic growth, and treatment. *Tumor Microenvironment*, 2013.
- [9] Geoffrey M. Cooper and Robert E. Hausman. *The Development and Causes of Cancer*. ASM Press, 2003.

- [10] K. M. Marien, V. Croons, Y. Waumans, E. Sluydts, S. De Schepper, L. Andries, W. Waelput, E. Fransen, P. B. Vermeulen, M. M. Kockx, and G. R De Meyer. Development and Validation of a Histological Method to Measure Microvessel Density in Whole-Slide Images of Cancer Tissue. *PLoS One*, 11(9):e0161496, Sept 2016.
- [11] BJ McGuire and TW Secomb. Estimation of capillary density in human skeletal muscle based on maximal oxygen consumption rates. *Am J Physiol Heart Circ Physiol*, 285(6):2382–91, dec 2003.
- [12] Ana Tellechea, Antonios Kafanas, Ermelindo Leal, Francesco Tecilazich, Sarada Kuchibhotla, Michael Auster, Iraklis Kontoes, Jacqueline Paolino, Eugénia Carvalho, Leena Pradhan, and Aristidis Veves. Increased skin inflammation and blood vessel density in human and experimental diabetes. *The international journal of lower extremity wounds*, 12, 02 2013.
- [13] TK Goldstick, VT Ciuryla, and L Zuckerman. Diffusion of oxygen in plasma and blood. *Adv Exp Med Biol*, 75:183–90, 1976.
- [14] Akitoshi Maeda, Yukiko Himeno, Masayuki Ikebuchi, Akinori Noma, and Akira Amano. Regulation of the glucose supply from capillary to tissue examined by developing a capillary model. *The Journal of Physiological Sciences*, 68(4):355–367, 2017.
- [15] K. Akons, E. J. Dann, and D. Yelin. Measuring blood oxygen saturation along a capillary vessel in human. *Biomedical optics express*, 8(11):5342–5348, 2017.
- [16] Timothy J. Strovas, Sarah C. Mcquaide, Judy B. Anderson, Vivek Nandakumar, Marina G. Kalyuzhnaya, Lloyd W. Burgess, Mark R. Holl, Deirdre R. Meldrum, and Mary E. Lidstrom. Direct measurement of oxygen consumption rates from attached and unattached cells in a reversibly sealed, diffusionaly isolated sample chamber. *Advances in Bioscience and Biotechnology*, 01(05):398–408, 2010.
- [17] Ioanna Papandreou, Rob A. Cairns, Lucrezia Fontana, Ai Lin Lim, and Nicholas C. Denko. Hif-1 mediates adaptation to hypoxia by actively downregulating mitochondrial oxygen consumption. *Cell Metabolism*, 3(3):187–197, 2006.
- [18] Francesca Maddalena, Giacomo Lettini, Rosj Gallicchio, Lorenza Sisinni, Vittorio Simeon, Anna Nardelli, Angela Assunta Venetucci, Giovanni Storto, and Matteo Landriscina. Evaluation of glucose uptake in normal and cancer cell lines by positron emission tomography. *Molecular imaging*, 14(9):7290–2015, 2015.
- [19] Anaira C Clavo, Raya S Brown, and Richard L Wahl. Fluorodeoxyglucose uptake in human cancer cell lines is increased by hypoxia. *Journal of nuclear medicine*, 36(9):1625–1632, 1995.
- [20] Mohamed Hassanein, Brandy Weidow, Elizabeth Koehler, Naimish Bakane, Shawn Garbett, Yu Shyr, and Vito Quaranta. Development of high-throughput quantitative assays for glucose uptake in cancer cell lines. *Molecular imaging and biology*, 13(5):840–852, 2011.
- [21] Saeed Ashrafinia, Hassan Mohy ud Din, Nicolas A Karakatsanis, Abhinav K Jha, Michael E Casey, Dan J Kadrimas, and Arman Rahmim. Generalized psf modeling for optimized quantitation in pet imaging. *Physics in Medicine Biology*, 62(12):5149, may 2017.
- [22] Chun-Yi Lin, Hueisch-Jy Ding, Cheng-Chieh Lin, Cheng-Chieh Chen, Shung-Shung Sun, and Chia-Hung Kao. Impact of age on fdg uptake in the liver on pet scan. *Clinical Imaging*, 34(5):348–350, 2010.

- [23] Eleonore H de Groot, Nieky Post, Ronald Boellaard, Nils R L Wagenaar, Antoon T M Willemsen, and Jorn A van Dalen. Optimized dose regimen for whole-body FDG-PET imaging. *EJNMMI Res.*, 3(1):63, 2013.
- [24] Joost J.M. van Griethuysen, Andriy Fedorov, Chintan Parmar, Ahmed Hosny, Nicole Aucoin, Vivek Narayan, Regina G.H. Beets-Tan, Jean-Christophe Fillion-Robin, Steve Pieper, and Hugo J.W.L. Aerts. Computational Radiomics System to Decode the Radiographic Phenotype. *Cancer Res.*, 77(21):e104–e107, nov 2017.
- [25] Alex Zwanenburg, Martin Vallières, Mahmoud A. Abdallah, Hugo J. W. L. Aerts, Vincent Andreczyk, Aditya Apte, Saeed Ashrafinia, Spyridon Bakas, Roelof J. Beuvinga, Ronald Boellaard, Marta Bogowicz, Luca Boldrini, Irène Buvat, Gary J. R. Cook, Christos Davatzikos, Adrien Depeursinge, Marie-Charlotte Desserot, Nicola Dinapoli, Cuong Viet Dinh, Sebastian Echegaray, Issam El Naqa, Andriy Y. Fedorov, Roberto Gatta, Robert J. Gillies, Vicky Goh, Michael Götz, Matthias Guckenberger, Sung Min Ha, Mathieu Hatt, Fabian Isensee, Philippe Lambin, Stefan Leger, Ralph T.H. Leijenaar, Jacopo Lenkowicz, Fiona Lippert, Are Losnegård, Klaus H. Maier-Hein, Olivier Morin, Henning Müller, Sandy Napel, Christophe Nioche, Fanny Orlhac, Sarthak Pati, Elisabeth A.G. Pfaehler, Arman Rahmim, Arvind U.K. Rao, Jonas Scherer, Muhammad Musib Siddique, Nanna M. Sijtsema, Jairo Socarras Fernandez, Emiliano Spezi, Roel J.H.M. Steenbakkers, Stephanie Tanadini-Lang, Daniela Thorwarth, Esther G.C. Troost, Taman Upadhaya, Vincenzo Valentini, Lisanne V. van Dijk, Joost van Griethuysen, Floris H.P. van Velden, Philip Whybra, Christian Richter, and Steffen Löck. The Image Biomarker Standardization Initiative: Standardized Quantitative Radiomics for High-Throughput Image-based Phenotyping. *Radiology*, 295(2):328–338, may 2020.
- [26] R Hi Thomlinson and LH Gray. The histological structure of some human lung cancers and the possible implications for radiotherapy. *British journal of cancer*, 9(4):539, 1955.
- [27] Xun Hu, Ming Chao, and Hao Wu. Central role of lactate and proton in cancer cell resistance to glucose deprivation and its clinical translation. *Signal transduction and targeted therapy*, 2(1):1–8, 2017.
- [28] Liqiang Zhang, Fengyu Su, Sean Buizer, Xiangxing Kong, Fred Lee, Kevin Day, Yanqing Tian, and Deirdre R Meldrum. A polymer-based ratiometric intracellular glucose sensor. *Chemical Communications*, 50(52):6920–6922, 2014.